Nano Research 2017, 10(5): 1794–1803
DOI 10.1007/s12274-017-1501-y
Research Article

ISSN 1998-0124
CN 11-5974/O4

Simple synthesis of a porous Sb/Sb_2O_3 nanocomposite for a high-capacity anode material in Na-ion batteries

Jun Pan[1], Nana Wang[1,†], Yanli Zhou[1,‡], Xianfeng Yang[2], Wenyao Zhou[3], Yitai Qian[1,4] (✉), and Jian Yang[1] (✉)

[1] *Key Laboratory of Colloid and Interface Chemistry, Ministry of Education, School of Chemistry and Chemical Engineering, Shandong University, Jinan 250100, China*
[2] *Analytical and Testing Center, South China University of Technology, Guangzhou 510640, China*
[3] *Jinan Licheng No.2 High School, Jinan 250105, China*
[4] *Department of Chemistry, Hefei National Laboratory for Physical Sciences at Microscale, University of Science and Technology of China, Hefei 230026, China*
[†] *Present address: College of Materials Science and Engineering, Taiyuan University of Technology, Taiyuan 030024, China*
[‡] *Present address: School of Environment and Material Engineering, Yantai University, Yantai 264005, China*

Received: 5 September 2016
Revised: 18 January 2017
Accepted: 31 January 2017

KEYWORDS

Sb/Sb_2O_3,
high-capacity,
anode material,
sodium ion batteries

ABSTRACT

High-capacity anode materials are highly desirable for sodium ion batteries. Here, a porous Sb/Sb_2O_3 nanocomposite is successfully synthesized by the mild oxidization of Sb nanocrystals in air. In the composite, Sb contributes good conductivity and Sb_2O_3 improves cycling stability, particularly within the voltage window of 0.02–1.5 V. It remains at a reversible capacity of 540 $mAh\cdot g^{-1}$ after 180 cycles at 0.66 $A\cdot g^{-1}$. Even at 10 $A\cdot g^{-1}$, the reversible capacity is still preserved at 412 $mAh\cdot g^{-1}$, equivalent to 71.6% of that at 0.066 $A\cdot g^{-1}$. These results are much better than Sb nanocrystals with a similar size and structure. Expanding the voltage window to 0.02–2.5 V includes the conversion reaction between Sb_2O_3 and Sb into the discharge/charge profiles. This would induce a large volume change and high structure strain/stress, deteriorating the cycling stability. The identification of a proper voltage window for Sb/Sb_2O_3 paves the way for its development in sodium ion batteries.

1 Introduction

Lithium ion batteries (LIBs) are efficient energy storage devices, and have been widely employed in consumer electronics, hybrid electric vehicles (EVs), and so on [1–3]. However, large-scale use of LIBs in these applications creates a serious issue, because lithium resources on earth are limited and unable to cover all the future demands. To address this concern, sodium ion batteries (NIBs) have come into sight, due to the high abundance and low cost of sodium. Moreover, NIB cell configurations and charge/discharge mechanisms are similar to those of LIBs, which allows them to follow in the footsteps of the lithium

---

Address correspondence to Jian Yang, yangjian@sdu.edu.cn; Yitai Qian, ytqian@ustc.edu.cn

predecessor for high performance. Although heavy sodium ions cause sluggish kinetics and the low voltages of electrode materials (vs. Na^+/Na) reduce energy density, NIBs are still very competitive in grid storage, where size and weight are not crucial factors.

Compared with cathode materials, the progress on the anode side is much less. Sodium cannot be directly used as the anode due to the safety concerns arising from its low melting point (97.7 °C), potential for dendrite formation, etc. [4, 5]. Although Na^+ ions can intercalate into hard carbon, it has a very low discharge voltage (<0.1 V) [6], which also raises the severe safety concern of the formation of sodium dendrites. Moreover, its capacity is quite limited (~200 $mAh \cdot g^{-1}$) [7]. Thus, it is necessary to seek other materials for the anode. Recently, Sb has attracted intense interest as a promising anode candidate, owing to its high theoretical capacity (660 $mAh \cdot g^{-1}$) [8], small electrode polarization (~0.25 V), moderate discharge voltage (0.5–0.8 V) [9], etc. But it experiences huge volume changes upon cycling that generate vast strain/stress, particle cracks, and structure failure. To address this issue, various strategies have been borrowed from the LIB system, such as structure engineering (porous or hollow structures) [10, 11], size control (via nanoparticles or nanotubes) [8, 12], surface modification (C or TiO_2 coatings) [13–22], and component modulation (MSb alloys, where M = Zn, Sn, Bi, Ni, etc.) [23–30]. In spite of this, improving cycling stability without the expense of capacity is still a great challenge.

Recently, the reversible conversion reaction between Sb_2O_3 and Sb was observed in NIBs [31], in addition to the alloying/dealloying reaction of Sb with Na. This result indicates the high theoretical capacity of Sb_2O_3 (1,103 $mAh \cdot g^{-1}$), but its poor conductivity retards charge-transfer kinetics and degrades electrochemical performance. Thus, highly conductive metallic Sb is associated with Sb_2O_3 to improve reaction kinetics, which has been discussed only in a few reports to date. The first work involving Sb/Sb_2O_3 as an anode material in NIBs was from Wang and coworkers [32]. They anchored Sb/Sb_2O_3 nanoparticles on a carbon sheet network (CSN) by plasma-enhanced chemical vapor deposition, followed by the growth of graphene onto the composite. Cyclic voltammetry (CV) and *ex situ* X-ray diffraction (XRD) patterns indicated that Sb could be further oxidized into Sb_2O_3 after charging to 2.0 V. In this voltage window (0–2.0 V), Sb/Sb_2O_3@graphene-CSN could deliver a capacity of about 221 $mAh \cdot g^{-1}$ at 5 $A \cdot g^{-1}$. Hong and Kwon reported morula-like Sb/Sb_2O_3 particles that were directly grown on the current collector via an electrodeposition method [33]. Raman spectroscopy also confirmed the reversible reaction between Sb and Sb_2O_3 as the composite was charged back to 2.5 V. The capacity remained ca. 212 $mAh \cdot g^{-1}$ for 3.3 $A \cdot g^{-1}$. Later, the same group synthesized a porous Sb/Sb_2O_3 composite grown on polypyrrole nanowires by a similar method [34]. They controlled the voltage window between 0.001–1.5 V, thus inhibiting the reversible reaction between Sb_2O_3 and Sb. However, this composite showed a higher reversible capacity of 300 $mAh \cdot g^{-1}$ at 3.3 $A \cdot g^{-1}$. Because the above two composites are different in size, shape, structure, and components, it cannot be concluded that the narrow voltage window works better for Sb/Sb_2O_3. But the effect of the voltage window on the performance of Sb/Sb_2O_3 definitely deserves to be studied in detail. If the low cut-off charge voltage inhibits this reaction, what is the role of Sb_2O_3 in this cycling? Could it help the electrochemical performance of Sb? In order to clarify these points, the same composite of Sb/Sb_2O_3 should be measured over different voltage windows for NIBs. Then, the underlying role of Sb_2O_3 needs to be explored. Finally, if Sb/Sb_2O_3 could combine Sb_2O_3 with other strategies (porous structure, nanoscale size), high performance would be expected.

Herein, a porous Sb/Sb_2O_3 nanocomposite is synthesized by thermal treatment of highly aggregated Sb nanocrystals in air. The presence of Sb_2O_3 in the nanocomposite is confirmed by its XRD pattern, Raman spectrum, and high-resolution transmission electron microscopy (HRTEM) image. Electrochemical measurements over different voltage windows confirm that the narrow voltage window (0.02–1.5 V) gives a better cycling stability and capacity retention than the broad one (0.02–2.5 V). It could deliver a capacity of 540 $mAh \cdot g^{-1}$ after 180 cycles at 0.66 $A \cdot g^{-1}$. Even at 10 $A \cdot g^{-1}$, the reversible capacity could still be maintained at 412 $mAh \cdot g^{-1}$, equivalent to 71.6% of the capacity at 0.066 $A \cdot g^{-1}$. This result is much better than most of the reported data on Sb anodes. Electrochemical impedance spectroscopy (EIS) shows that the cycled Sb/Sb_2O_3 electrode exhibits reduced surface film and charge-transfer resistances, thereby improving the electrochemical performance.

2 Experimental

2.1 Material synthesis

All the reagents were purchased and used without purification. Typically, 0.91 mg of $NaBH_4$ (96%, Sinopharm) was dissolved in 25 mL N-methyl-2-pyrrolidone (NMP, 98%, Aladdin) at room temperature. Then, the solution was heated to 60 °C under N_2, accompanied by vigorous stirring. After 5.0 mL of 6 mM $SbCl_3$ (99%, Aladdin) was injected into the NMP, the solution immediately became black, suggesting the formation of Sb nanoparticles. The solution was quickly immersed in an ice/water bath to inhibit the continuous growth of Sb. The powder was collected by centrifugation, washed several times with absolute ethanol, and dried at 70 °C in a vacuum overnight. The as-obtained Sb nanoparticles were kept at 100 °C in air for 3 h to achieve oxidation, generating porous Sb/Sb_2O_3 nanoparticles.

2.2 Material characterization

XRD patterns were obtained from an X-ray diffractometer (Bruker D8 Adv., Germany), using a monochromatic Cu-Kα line as a radiation source. Scanning electron microscope (SEM) images were collected on a field-emission scanning electron microscope (SUPRA 55 SAPPHIRE, Germany). Transmission electron microscope (TEM) images, high-resolution TEM (HRTEM) images and energy dispersive X-ray spectra (EDX) were taken with a transmission electron microscope (JEOL JEM 1011, or JEOL JEM-2100F, Japan). Raman spectra were measured on a NEXUS 670 Raman spectrometer using an excitation wavelength of 632 nm. Nitrogen sorption isotherm measurements were performed on a gas sorptometer (Micromeritics ASAP 2020 HD88, USA) at 77.3 K. Thermal gravimetric analysis (TGA) was achieved in air at a heating rate of 10 °C·min^{-1} on a thermal analyzer (Mettler Toledo TGA/SDTA851, Switzerland).

2.3 Electrochemical measurements

The electrochemical performance of Sb/Sb_2O_3 as an NIB anode material was tested with CR2032 coin cells. Firstly, the working electrode was made of 65 wt.% of the active material, 20 wt.% of acetylene black, and 15 wt.% of sodium alginate (SA). These components were milled for 30 min with droplets of deionized water, resulting in a viscous slurry. The slurry was spread on a clean copper foil by a blade, and dried under vacuum at 60 °C for 8 h. The loading mass of the active material was ca. 0.9–1.2 mg·cm^{-2}. Then, the working electrode was punched into disks with diameters of 1.2 cm. Coin cells were assembled using these disks within an Ar-filled glovebox (Mikrouna, Super 1220/750/900). Na foil was used as the counter and reference electrode, Whatman GF/F glass microfibers functioned as the separator, and the electrolyte was comprised of 1.0 M $NaClO_4$ in ethylene carbonate and diethyl carbonate (EC and DEC, volume ratio of 1:1) containing 10% fluoroethylene carbonate (FEC). CVs of these coin cells were collected on an electrochemical workstation (LK2005A, China) within 0.02–2.5 V. Discharge/charge profiles were examined on Land battery cyclers (LAND CT 2001A, China). EIS was measured by an electrochemical workstation (Autolab PGSTAT 302N) in the frequency range of 100 kHz to 0.01 Hz.

3 Results and discussion

Sb/Sb_2O_3 was prepared by the reduction of $SbCl_3$ with $NaBH_4$, followed by oxidation in air (Fig. 1). As an intermediate product, these Sb nanocrystals directly affect the size and shape of Sb/Sb_2O_3. The as-obtained Sb nanocrystals are aggregated nanoparticles with diameters over 40–140 nm (Figs. S1 and S2 in the

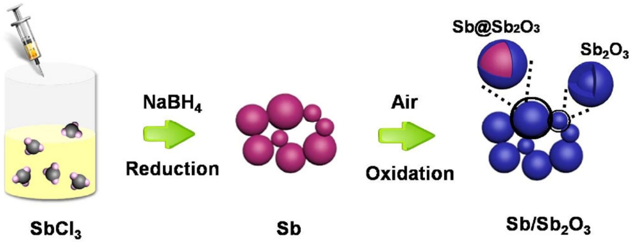

Figure 1 The preparation of Sb/Sb_2O_3 nanoparticles.

Electronic Supplementary Material (ESM)). After this oxidization, some Sb nanoparticles are completely converted to Sb_2O_3 whilst others only have the surface oxidized, which can be ascribed to the low reaction temperature of 100 °C. The nanoparticles coalesce together, forming robust connections. High temperatures would markedly promote the content of Sb_2O_3 in the composite (Fig. S3 in the ESM). The coexistence of Sb_2O_3 with Sb is also supported by the Raman spectra (Fig. 2(b)), where the peaks at 190 and 253 cm^{-1} come from Sb_2O_3 [35], and the peaks at 115 and 152 cm^{-1} arise from Sb [36]. These results are in good agreement with those from the XRD pattern. The weight ratio of Sb to Sb_2O_3 was obtained from the EDX spectrum (Fig. 2(c)), and estimated to be 82.7:17.3. This result is also supported by TGA. As shown in Fig. 2(d), there are two stages of weight gain over 300–650 °C. The first between 300–450 °C is likely due to the complete oxidation of Sb to Sb_2O_3, which is confirmed by the disappearance of Sb in the product obtained at 500 °C (Fig. S4(a) in the ESM). Based on this weight gain, the weight ratio of Sb to Sb_2O_3 was calculated as 83.4:16.6, close to that obtained from the EDX spectrum. The second stage between 600 and 650 °C is ascribed to the further oxidation of Sb_2O_3 to Sb_2O_5, as evidenced in the XRD pattern (Fig. S4(b) in the ESM).

Figures 3(a) and 3(b) show SEM images of Sb/Sb_2O_3. It consists of highly aggregated nanoparticles, similar to the parent Sb nanocrystals. It is noted that this aggregation leaves a number of voids between neighboring nanoparticles, forming unique porous structures. These features can be visualized more clearly in the TEM images (Fig. 3(c)). As documented in many works on anode materials in LIBs and NIBs [37, 38], this porous structure would facilitate the electrolyte transport, lower the areal current density, and accommodate the volume change during sodiation/desodiation, improving the electrochemical performance. Nitrogen sorption isotherms were measured, as shown in Fig. S5 in the ESM. There is apparent sorption hysteresis, indicating the mesoporous structure. Most of the pore sizes range from 15 to 60 nm. This is comparable to the sizes of the primary Sb/Sb_2O_3 nanoparticles, which have an average size of 90 nm (Fig. 3(d)). In order to identify the distribution of Sb and Sb_2O_3 in the composite, a high angle annular dark field (HAADF)-scanning transmission electron microscopy (STEM) image was recorded (Fig. 3(e)), where Sb and Sb_2O_3 exhibit an obvious contrast due to their different electron-scattering abilities. Also, element mapping was conducted for the composite (Fig. S6 in the ESM).

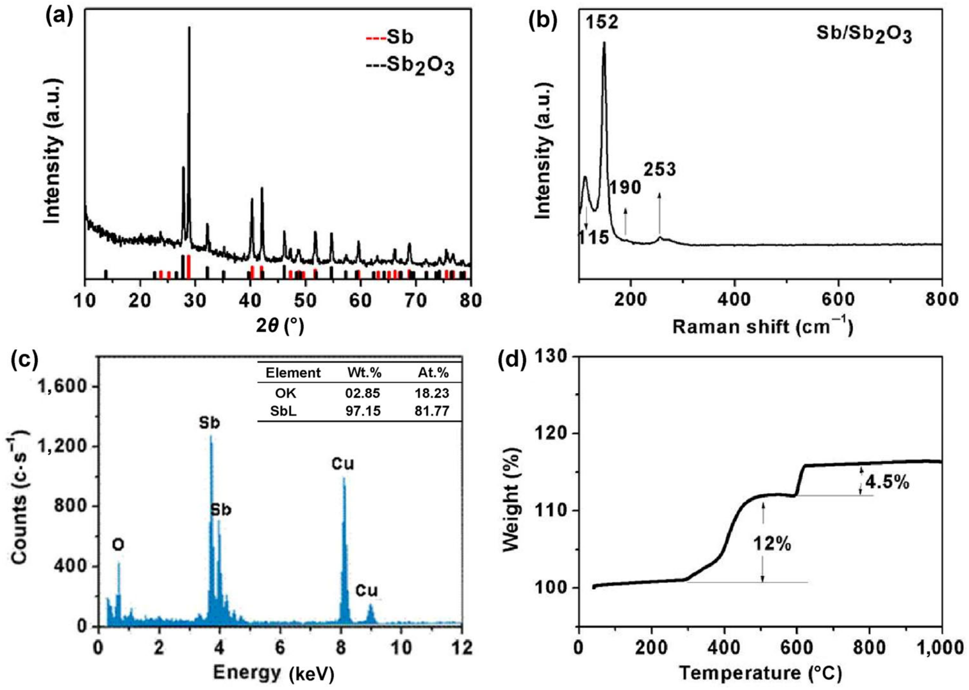

Element	Wt.%	At.%
OK	02.85	18.23
SbL	97.15	81.77

Figure 2 (a) XRD pattern of Sb/Sb_2O_3. (b) Raman spectrum of Sb/Sb_2O_3. (c) EDX spectrum of Sb/Sb_2O_3. (d) TGA of Sb/Sb_2O_3 in air.

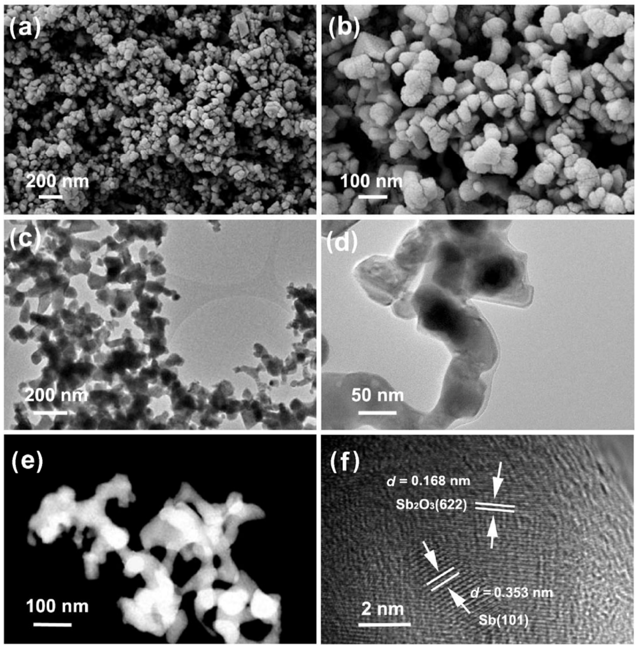

Figure 3 (a) and (b) SEM images of Sb/Sb_2O_3. (c) and (d) TEM images of Sb/Sb_2O_3. (e) HADDF-STEM image of Sb/Sb_2O_3. (f) HRTEM image of Sb/Sb_2O_3.

Oxygen is located either on the particle surface (Site I) or gray areas (Site II). The former (Site I) can be ascribed to the surface oxidation of Sb, particularly for the nanoparticles. The latter (Site II) can be explained by the formation of Sb_2O_3, consistent with the low intensity of Sb there. These results indicate that Sb is blended with Sb_2O_3 in the composite, but the surfaces are covered by oxide. The HRTEM image (Fig. 3(f)) shows clear lattice fringes of 0.353 nm from the (101) crystal planes of Sb and 0.168 nm from the (622) crystal planes of Sb_2O_3, suggesting their intimate contact.

CV curves of Sb/Sb_2O_3 nanocrystals were measured over the range of 0.02–2.5 V at a scan rate of 0.1 mV·s^{-1}. As shown in Fig. 4(a), the first cathodic scan displays one weak peak at 1.07 V and one intense weak peak over 0.2–0.7 V. The former is likely due to the reduction of Sb_2O_3 to Sb [39]. The latter is attributed to the formation of a solid-electrolyte interphase (SEI) film and the insertion of Na into Sb [40, 41]. The first anodic scan indicates the consecutive oxidations of the Na_3Sb alloy, including the extraction of Na ions from the alloy (~0.87 V), and the conversion of Sb into oxides (1.2–2.2 V). The extremely small current and large width of the peak over 1.2–2.2 V (inset of Fig. 4(a)) can be ascribed to the partial reversibility of this oxidation and the low content of Sb_2O_3 in the composite. In the following cycles, the cathodic peak from the reduction of Sb_2O_3 at ~1.0 V remains, implying reversible conversion between Sb_2O_3 and Sb. This phenomenon has been observed in previous reports [32–34]. Meanwhile, there is a great change of the intense peak over 0.7–0.2 V. The three peaks at 0.72, 0.55, and 0.36 V indicate the stepwise reduction of Sb to NaSb, Na_xSb, and Na_3Sb [40]. This change suggests good kinetics inside the composite, as supported by the reduced electrode polarization compared to the first cycle. The anodic and cathodic peaks are then stable over further cycles, indicating the good electrochemical stability of Sb/Sb_2O_3.

Although the conversion reaction between Sb_2O_3 and Sb could increase the capacity, it would also induce a large volume change and high structure strain/stress, likely lowering the cycling stability. In order to confirm this point, Sb/Sb_2O_3 was cycled over two voltage windows. The wide voltage window (0.02–2.5 V) enables the reversible conversion reaction to occur, as supported by the charge plateau around 1.5–1.8 V (Fig. 4(b)) and HRTEM images of the electrode charged to 2.5 V (Figs. S7(a) and S7(b) in the ESM). The narrow voltage window (0.02–1.5 V) has less of these signs in the charge profile (Fig. 4(b)) and in the HRTEM images (Figs. S7(c) and S7(d) in the ESM). Thus, cycling over 0.02–2.5 V gives a higher initial coulombic efficiency (74.6%) than over 0.02–1.5 V (70.7%). The capacity loss in both cases could be correlated to the decomposition of electrolyte to form an SEI film, the partially reversible redox reaction between Sb and Sb_2O_3, and so on. In the following cycles, the Coulombic efficiency goes up to 98.8%, accompanied by the slight increase of reversible capacity for both cases (Fig. S8 in the ESM). This capacity gain occurs at the voltage range over 0.75–0.40 V, indicating that more sodium ions could be inserted at a relatively high voltage. It is believed that this activation might be associated with size reduction and structure rearrangement of active particles, due to conversion and alloy reactions.

Figure 4(c) shows the cycling of Sb and Sb/Sb_2O_3 over different voltage windows at a current density of 0.66 A·g^{-1}. It is found that cycling Sb/Sb_2O_3 between 0.02–2.5 V gradually increases the capacity over the

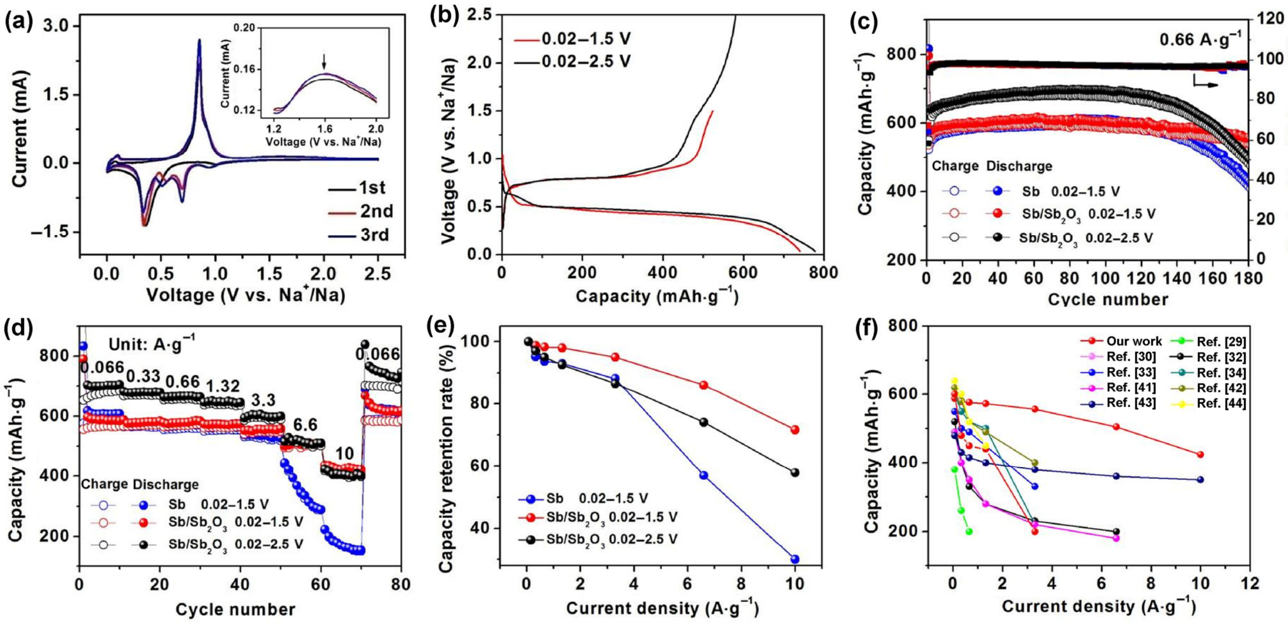

Figure 4 (a) Cyclic voltammograms for Sb/Sb_2O_3 at a scan rate of 0.1 $mV \cdot s^{-1}$ for the first three cycles. (b) Galvanostatic discharge/charge profiles of Sb/Sb_2O_3 over different voltage windows. (c) Cycling performance and (d) rate performance of Sb and Sb/Sb_2O_3. (e) Capacity retention of Sb and Sb/Sb_2O_3 at different current densities. (f) Comparison of different Sb-based electrodes.

first tens of cycles, which then levels off at 644 $mAh \cdot g^{-1}$. After 180 cycles, the capacity quickly drops to 481 $mAh \cdot g^{-1}$. Similar behavior is also demonstrated by Sb, though it shows a lower capacity throughout cycling because there is no reversible reaction between Sb_2O_3 and Sb. Compared with these cases, Sb/Sb_2O_3 cycled between 0.02–1.5 V shows an enhanced cycling stability, although the reversible capacity is not the highest of all the measurements. After 180 cycles, the capacity retention is ~92.8%, much higher than those of Sb (72.9%) and Sb/Sb_2O_3 cycled over 0.02–2.5 V (74.7%). This superior stability of Sb/Sb_2O_3 measured within 0.02–1.5 V is likely due to newly formed Na_2O buffering the strain/stress caused by the volume change and enhancing the structure stability (Fig. S9 in the ESM). Moreover, Na_2O will not be converted to Sb_2O_3 again, owing to the low cut-off charge voltage (Figs. S7(c) and S7(d) in the ESM). A similar stability enhancement within 0.02–1.5 V is also observed for Sb_2O_3 (Fig. S10 in the ESM). The effect of voltage window on rate capability is shown in Fig. 4(d), where Sb/Sb_2O_3 cycled between 0.02–2.5 V shows a higher capacity but lower capacity retention than that cycled between 0.02–1.5 V. Notably, both of them are much better than Sb. Sb/Sb_2O_3 showed reversible capacity values of 575, 568, 565, 563, 547, 495, and 412 $mAh \cdot g^{-1}$ at rates of 0.066, 0.33, 0.66, 1.32, 3.3, 6.6, and 10 $A \cdot g^{-1}$, respectively, for the voltage window of 0.02–1.5 V. After the current density was reduced to 0.066 $A \cdot g^{-1}$, the capacity could be completely recovered. The good capacity retention of Sb/Sb_2O_3 cycled over 0.02–1.5 V is shown in Fig. 4(e), indicating the fast kinetics of the electrochemical reactions. Its capacity at 10 $A \cdot g^{-1}$ is approximately 71.6% of that at 0.066 $A \cdot g^{-1}$, even though the current density was increased by 150 times. Compared with previous reports, this performance of Sb/Sb_2O_3 is much higher (Fig. 4(f)) [29, 30, 32–34, 41–44]. Sb/Sb_2O_3@graphene-CSN, prepared by plasma-enhanced chemical vapor deposition and the growth of graphene onto the composite, only exhibited a capacity about 221 $mAh \cdot g^{-1}$ at 5 $A \cdot g^{-1}$ [32]. Morula-like Sb/Sb_2O_3 particles, grown on the current collector via an electrodeposition process, presented a capacity of 212 $mAh \cdot g^{-1}$ at 3.3 $A \cdot g^{-1}$ [33]. Even for associated Sb/Sb_2O_3 with polypyrrole nanowires, the capacity was still ~300 $mAh \cdot g^{-1}$ for 3.3 $A \cdot g^{-1}$ [34].

EIS of the electrodes made of Sb/Sb_2O_3 and Sb were measured to gain insight into the underlying role of Sb_2O_3. Because Sb/Sb_2O_3 cycled between 0.02–1.5 V shows the best results, it is discussed here in comparison with Sb. As shown in Fig. 5(a), the EIS spectra of both Sb and Sb/Sb_2O_3 exhibit a heavily depressed semicircle, followed by diffusion drift. The spectra could be simulated by a modified equivalent circuit, as presented in the inset of Fig. 5(a). Here, R_s indicates the resistance of the electrolyte and cell components. R_f refers to the resistance related to the surface film, including the SEI film, on the electrode. R_{ct} represents the charge-transfer resistance at the electrolyte/surface film/electrode interfaces. Rather than pure capacitances, constant phase elements (CPEs) fit the depressed semicircle, which arises from the inhomogeneous nature of the composite (Table S1 in the ESM). On the basis of this circuit, it is found that Sb/Sb_2O_3 at the open-circuit voltage has a larger R_{ct} and a smaller R_f than Sb. This result can be attributed to Sb_2O_3 on the composite. It is probable that the poor conductivity of Sb_2O_3 retards the charge-transfer transportation, thus increasing R_{ct}. As the same time, the presence of Sb_2O_3 also affects the formation of the surface film, resulting in the decrease of R_f. However, how Sb_2O_3 affects the surface film, and how this film reduces R_f, is still not understood. After 100 cycles between 0.02–1.5 V (Fig. 5(b)), R_f and R_{ct} of Sb and Sb/Sb_2O_3 decrease significantly. This decrease is ascribed to the size reduction of primary particles caused by alloying/dealloying processes. Meanwhile, both R_f and R_{ct} values of Sb/Sb_2O_3 are smaller than those of Sb, consistent with the superior electrochemical performance of Sb/Sb_2O_3.

The ratio of Sb/Sb_2O_3 in the composite could be tuned by controlling the oxidation temperature. At 100 °C, the content of Sb_2O_3 in the product is ~17%, based on the EDX spectra. At 200 °C, this content rises to 35%. The cycling performance of the two composites and metallic Sb were compared. As shown in Fig. 6, the composite with 17% Sb_2O_3 shows the best performance. Without Sb_2O_3 in the composite, the capacity degrades upon cycling. The high content of Sb_2O_3 lowers the specific capacity. So, of these three materials, that with 17% Sb_2O_3 shows the best performance.

4 Conclusion

In summary, a porous Sb/Sb_2O_3 nanocomposite has been successfully synthesized by the mild oxidation of highly aggregated Sb nanocrystals. In this composite, Sb offers good conductivity and high capacity. Sb_2O_3 forms Na_2O upon sodiation, which buffers the volume change and enhances the cycling stability. Together with the advantages of its porous structure, this nanocomposite exhibits excellent electrochemical performance as an anode material for NIBs. It was found that the nanocomposite exhibits better cycling stability and rate capability within the voltage window of 0.02–1.5 V. It could deliver a capacity of 540 mAh·g^{-1} after 180 cycles at 0.66 A·g^{-1}. Even at 10 A·g^{-1}, the reversible capacity could be maintained at 412 mAh·g^{-1}, equivalent to 71.6% of the capacity at 0.066 A·g^{-1}. These results are much better than the reported NIB anode materials. Expanding the voltage window to 0.02–2.5 V includes the conversion reaction between Sb_2O_3 and Sb in the discharge/charge profiles. This would induce a large volume change and high structure strain/stress, deteriorating the cycling stability.

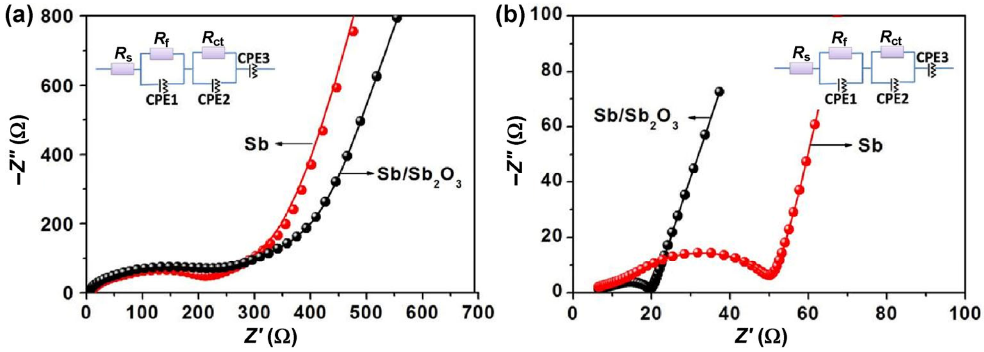

Figure 5 (a) Nyquist plots of Sb/Sb_2O_3 and Sb at the open-circuit voltage. (b) Sb/Sb_2O_3 and Sb charged to 1.5 V after 100 cycles.

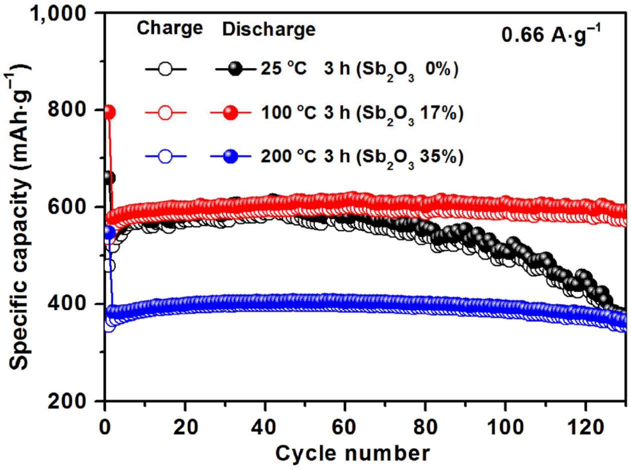

Figure 6 Cycling performance of Sb/Sb_2O_3 composites with different contents of Sb_2O_3 between 0.02–1.5 V.

EIS spectra demonstrated that Sb/Sb_2O_3 could effectively reduce the resistances of the surface film and charge-transfer upon cycling, resulting in superior electrochemical properties.

Acknowledgements

This work was supported by National Nature Science Foundation of China (No. 21471090 and 61527809), and Taishan Scholarship in Shandong Provinces (No. ts201511004), and Shandong Provincial Nature Science Foundation for Distinguished Young Scholar (No. JQ2012 05). We also want to thank Prof. Chunjiang Jia for his help on BET measurements.

Electronic Supplementary Material: Supplementary material (XRD pattern and TEM images of Sb nanoparticles; XRD patterns of the products obtained by thermal treatment of Sb or Sb/Sb_2O_3 at different temperatures; N_2 adsorption–desorption isotherms and pore size distribution of Sb/Sb_2O_3, HADDF images and element mapping of Sb/Sb_2O_3, HRTEM images of Sb/Sb_2O_3 nanocomposite charged to 2.5 V and 1.5 V; galvanostatic discharge/charge profiles of Sb/Sb_2O_3 cycled between 0.02–1.5 V or 0.02–2.5 V; SEM images of Sb and Sb/Sb_2O_3 nanocomposite after 100 cycles; cycling performances of Sb_2O_3 in different voltage windows; as well as fitting data of Sb/Sb_2O_3 in equivalent circuit) is available in the online version of this article at http://dx.doi.org/10.1007/s12274-017-1501-y.

References

[1] Ji, L. W.; Rao, M. M.; Aloni, S.; Wang, L.; Cairns, E. J.; Zhang, Y. G. Porous carbon nanofiber–sulfur composite electrodes for lithium/sulfur cells. *Energy Environ. Sci.* **2011**, *4*, 5053–5059.

[2] Wang, H. K.; Lu, X.; Li, L. C.; Li, B. B.; Cao, D. X.; Wu, Q. Z.; Li, Z. H.; Yang, G.; Guo, B. L.; Niu, C. M. Synthesis of SnO_2 versus Sn crystals within N-doped porous carbon nanofibers via electrospinning towards high-performance lithium ion batteries. *Nanoscale* **2016**, *8*, 7595–7603.

[3] Xing, Z.; Ju, Z. C.; Yang, J.; Xu, H. Y.; Qian, Y. T. One-step hydrothermal synthesis of $ZnFe_2O_4$ nano-octahedrons as a high capacity anode material for Li-ion batteries. *Nano Res.* **2012**, *5*, 477–485.

[4] Sun, Y.; Zhao, L.; Pan, H. L.; Lu, X.; Gu, L.; Hu, Y. S.; Li, H.; Armand, M.; Ikuhara, Y.; Chen, L. Q. et al. Direct atomic-scale confirmation of three-phase storage mechanism in $Li_4Ti_5O_{12}$ anodes for room-temperature sodium-ion batteries. *Nat. Commun.* **2013**, *4*, 1870.

[5] Hong, Z. S.; Zhou, K. Q.; Huang, Z. G.; Wei, M. D. Iso-oriented anatase TiO_2 mesocages as a high performance anode material for sodium-ion storage. *Sci. Rep.* **2015**, *5*, 11960.

[6] Cao, Y. L.; Xiao, L. F.; Sushko, M. L.; Wang, W.; Schwenzer, B.; Xiao, J.; Nie, Z. M.; Saraf, L. V.; Yang, Z. G.; Liu, J. Sodium ion insertion in hollow carbon nanowires for battery applications. *Nano Lett.* **2012**, *12*, 3783–3787.

[7] Legrain, F.; Sottmann, J.; Kotsis, K.; Gorantla, S.; Sartori, S.; Manzhos, S. Amorphous (glassy) carbon, a promising material for sodium ion battery anodes: A combined first-principles and experimental study. *J. Phys. Chem. C* **2015**, *119*, 13496–13501.

[8] Wang, N. N.; Bai, Z. C.; Qian, Y. T.; Yang, J. Double-walled Sb@TiO_{2-x} nanotubes as a superior high-rate and ultralong-lifespan anode material for Na-ion and Li-ion batteries. *Adv. Mater.* **2016**, *28*, 4126–4133.

[9] Baggetto, L.; Ganesh, P.; Sun, C. N.; Meisner, R. A.; Zawodzinski, T. A.; Veith, G. M. Intrinsic thermodynamic and kinetic properties of Sb electrodes for Li-ion and Na-ion batteries: Experiment and theory. *J. Mater. Chem. A* **2013**, *1*, 7985–7994.

[10] Hou, H. S.; Jing, M. J.; Yang, Y. C.; Zhu, Y. R.; Fang, L. B.; Song, W. X.; Pan, C. C.; Yang, X. M.; Ji, X. B. Sodium/lithium storage behavior of antimony hollow nanospheres for rechargeable batteries. *ACS Appl. Mater. Interfaces* **2014**, *6*, 16189–16196.

[11] Kim, H.; Cho, J. Template synthesis of hollow Sb nanoparticles as a high-performance lithium battery anode material.

Chem. Mater. **2008**, *20*, 1679–1681.

[12] Walter, M.; Erni, R.; Kovalenko, M. V. Inexpensive antimony nanocrystals and their composites with red phosphorus as high-performance anode materials for Na-ion batteries. *Sci. Rep.* **2015**, *5*, 8418.

[13] Wu, L.; Hu, X. H.; Qian, J. F.; Pei, F.; Wu, F. Y.; Mao, R. J.; Ai, X. P.; Yang, H. X.; Cao, Y. L. Sb–C nanofibers with long cycle life as an anode material for high-performance sodium-ion batteries. *Energy Environ. Sci.* **2014**, *7*, 323–328.

[14] Zhu, Y. J.; Han, X. G.; Xu, Y. H.; Liu, Y. H.; Zheng, S. Y.; Xu, K.; Hu, L. B.; Wang, C. S. Electrospun Sb/C fibers for a stable and fast sodium-ion battery anode. *ACS Nano* **2013**, *7*, 6378–6386.

[15] Zhang, N.; Liu, Y. C.; Lu, Y. Y.; Han, X. P.; Cheng, F. Y.; Chen, J. Spherical nano-Sb@C composite as a high-rate and ultra-stable anode material for sodium-ion batteries. *Nano Res.* **2015**, *8*, 3384–3393.

[16] Wang, M.; Yang, Z. Z.; Wang, J. Q.; Li, W. H.; Gu, L.; Yu, Y. Sb nanoparticles encapsulated in a reticular amorphous carbon network for enhanced sodium storage. *Small* **2015**, *11*, 5381–5387.

[17] Qiu, S.; Wu, X. Y.; Xiao, L. F.; Ai, X. P.; Yang, H. X.; Cao, Y. L. Antimony nanocrystals encapsulated in carbon microspheres synthesized by a facile self-catalyzing solvothermal method for high-performance sodium-ion battery anodes. *ACS Appl. Mater. Interfaces* **2016**, *8*, 1337–1343.

[18] Zhou, X. L.; Zhong, Y. R.; Yang, M.; Hu, M.; Wei, J. P.; Zhou, Z. Sb nanoparticles decorated N-rich carbon nanosheets as anode materials for sodium ion batteries with superior rate capability and long cycling stability. *Chem. Commun.* **2014**, *50*, 12888–12891.

[19] Nithya, C.; Gopukumar, S. rGO/nano Sb composite: A high performance anode material for Na^+ ion batteries and evidence for the formation of nanoribbons from the nano rGO sheet during galvanostatic cycling. *J. Mater. Chem. A* **2014**, *2*, 10516–10525.

[20] Hou, H. S.; Jing, M. J.; Yang, Y. C.; Zhang, Y.; Song, W. X.; Yang, X. M.; Chen, J.; Chen, Q. Y.; Ji, X. B. Antimony nanoparticles anchored on interconnected carbon nanofibers networks as advanced anode material for sodium-ion batteries. *J. Power Sources* **2015**, *284*, 227–235.

[21] Li, K. F.; Su, D. W.; Liu, H.; Wang, G. X. Antimony-carbon-graphene fibrous composite as freestanding anode materials for sodium-ion batteries. *Electrochim. Acta* **2015**, *177*, 304–309.

[22] Zhang, W.; Liu, Y. T.; Chen, C. J.; Li, Z.; Huang, Y. H.; Hu, X. L. Flexible and binder-free electrodes of Sb/rGO and $Na_3V_2(PO_4)_3$/rGO nanocomposites for sodium-ion batteries. *Small* **2015**, *11*, 3822–3829.

[23] Li, L.; Seng, K. H.; Li, D.; Xia, Y. Y.; Liu, H. K.; Guo, Z. P. SnSb@carbon nanocable anchored on graphene sheets for sodium ion batteries. *Nano Res.* **2014**, *7*, 1466–1476.

[24] Jackson, E. D.; Green, S.; Prieto, A. L. Electrochemical performance of electrodeposited Zn_4Sb_3 films for sodium-ion secondary battery anodes. *ACS Appl. Mater. Interfaces* **2015**, *7*, 7447–7450.

[25] Darwiche, A.; Toiron, M.; Sougrati, M. T.; Fraisse, B.; Stievano, L.; Monconduit, L. Performance and mechanism of $FeSb_2$ as negative electrode for Na-ion batteries. *J. Power Sources* **2015**, *280*, 588–592.

[26] Baggetto, L.; Marszewski, M.; Górka, J.; Jaroniec, M.; Veith, G. M. AlSb thin films as negative electrodes for Li-ion and Na-ion batteries. *J. Power Sources* **2013**, *243*, 699–705.

[27] Allcorn, E.; Manthiram, A. NiSb-Al_2O_3-C nanocomposite anodes with long cycle life for Li-ion batteries. *J. Phys. Chem. C* **2014**, *118*, 811–822.

[28] Zhao, Y. B.; Manthiram, A. High-capacity, high-rate Bi-Sb alloy anodes for lithium-ion and sodium-ion batteries. *Chem. Mater.* **2015**, *27*, 3096–3101.

[29] Nam, D. H.; Hong, K. S.; Lim, S. J.; Kwon, H. S. Electrochemical synthesis of a three-dimensional porous Sb/Cu_2Sb anode for Na-ion batteries. *J. Power Sources* **2014**, *247*, 423–427.

[30] Liao, S.; Sun, Y.; Wang, J.; Cui, H.; Wang, C. X. Three dimensional self-assembly ZnSb nanowire balls with good performance as sodium ions battery anode. *Electrochim. Acta* **2016**, *211*, 11–17.

[31] Hu, M. J.; Jiang, Y. Z.; Sun, W. P.; Wang, H. T.; Jin, C. H.; Yan, M. Reversible conversion-alloying of Sb_2O_3 as a high-capacity, high-rate, and durable anode for sodium ion batteries. *ACS Appl. Mater. Interfaces* **2014**, *6*, 19449–19455.

[32] Li, N.; Liao, S.; Sun, Y.; Song, H. W.; Wang, C. X. Uniformly dispersed self-assembled growth of Sb_2O_3/Sb@graphene nanocomposites on a 3D carbon sheet network for high Na-storage capacity and excellent stability. *J. Mater. Chem. A* **2015**, *3*, 5820–5828.

[33] Hong, K. S.; Nam, D. H.; Lim, S. J.; Sohn, D. R.; Kim, T. H.; Kwon, H. S. Electrochemically synthesized Sb/Sb_2O_3 composites as high-capacity anode materials utilizing a reversible conversion reaction for Na-ion batteries. *ACS Appl. Mater. Interfaces* **2015**, *7*, 17264–17271.

[34] Nam, D. H.; Hong, K. S.; Lim, S. J.; Kim, M. J.; Kwon, H. S. High-performance Sb/Sb_2O_3 anode materials using a polypyrrole nanowire network for Na-ion batteries. *Small* **2015**, *11*, 2885–2892.

[35] Zhang, H. L.; Li, F.; Liu, C.; Tan, J.; Cheng, H. M. New insight into the solid electrolyte interphase with use of a focused ion beam. *J. Phys. Chem. B* **2005**, *109*, 22205–22211.

[36] Gómez-Cámer, J. L.; Villevieille, C.; Novák, P. Antimony based negative electrodes for next generation Li-ion batteries. *J. Mater. Chem. A* **2013**, *1*, 13011–13016.

[37] Wang, N. N.; Ma, X. J.; Xu, H. Y.; Chen, L.; Yue, J.; Niu, F. E.; Yang, J.; Qian, Y. T. Porous $ZnMn_2O_4$ microspheres as a promising anode material for advanced lithium-ion batteries. *Nano Energy* **2014**, *6*, 193–199.

[38] Wang, N. N.; Chen, L.; Ma, X. J.; Yue, J.; Niu, F. E.; Xu, H. Y.; Yang, J.; Qian, Y. T. Facile synthesis of hierarchically porous NiO micro-tubes as advanced anode materials for lithium-ion batteries. *J. Mater. Chem. A* **2014**, *2*, 16847–16850.

[39] Lewandowski, A.; Swiderska-Mocek, A.; Waliszewski, L. Solid electrolyte interphase formation on metallic lithium. *J. Solid State Electrochem.* **2012**, *16*, 3391–3397.

[40] Hui, J. S.; Burgess, M.; Zhang, J. R.; Rodríguez-López, J. Layer number dependence of Li^+ intercalation on few-layer graphene and electrochemical imaging of its solid−electrolyte interphase evolution. *ACS Nano* **2016**, *10*, 4248–4257.

[41] Yang, C. L.; Li, E. H.; Yang, Z. Z.; Gu, L.; Yu, Y. Nanoconfined antimony in sulfur and nitrogen co-doped three-dimensionally (3D) interconnected macroporous carbon for high-performance sodium-ion batteries. *Nano Energy* **2015**, *18*, 12–19.

[42] Liu, S.; Feng, J. K.; Bian, X. F.; Liu, J.; Xu, H. The morphology-controlled synthesis of a nanoporous-antimony anode for high-performance sodium-ion batteries. *Energy Environ. Sci.* **2016**, *9*, 1229–1236.

[43] Liu, Z. M.; Yu, X. Y.; Lou, X. W.; Paik, U. Sb@C coaxial nanotubes as a superior long-life and high-rate anode for sodium ion batteries. *Energy Environ. Sci.* **2016**, *9*, 2314–2318.

[44] Yang, Y. C.; Yang, X. M.; Zhang, Y.; Hou, H. S.; Jing, M. J.; Zhu, Y. R.; Fang, L. B.; Chen, Q. Y.; Ji, X. B. Cathodically induced antimony for rechargeable Li-ion and Na-ion batteries: The influences of hexagonal and amorphous phase. *J. Power Sources* **2015**, *282*, 358–367.